This article has been accepted for publication in IEEE Transactions on Transportation Electrification. This is the author's version which has not been fully edited and content may change prior to final publication. Citation information: DOI 10.1109/TTE.2022.3233538

Concept and Demonstration of a Coaxial Magnetic Coupling with Electromagnetic Disconnection for Aircraft Permanent Magnet Generators

O.R. Tweedy, Y. Akcay, P. Giangrande, *Senior Member, IEEE*, M. Galea, *Member, IEEE*

***Abstract*— The application of more electrified systems in aircraft is required to achieve the target of a more sustainable aviation industry. This in turn relies on the development of new electro-mechanical devices to ensure reliability of critical aircraft functions during flight. The aim of this work is to develop and test a device capable of protecting permanent magnet generators from damage, thus enabling the practical use of such high power density generators in aircraft while eliminating their inherent vulnerability to sustained electrical faults. A novel electromechanical actuator concept for decoupling a permanent magnetic generator from an aircraft gas turbine engine is introduced and experimentally validated. The proposed concept combines a coaxial magnetic coupling with an electromagnetic actuator, allowing for rapid disconnection in case of electrical fault detection. The 2D finite element magnetic analysis methodology employed in the design of the magnetic coupling and electromagnetic actuator is validated with experiments that reveal the peak torque results of the magnetic coupling are accurate to within a 2.5% error and the actuator can produce the 450 N pull force required for disconnection. The device is capable of operating at a maximum speed of 12,000 RPM and transmitting a load of 32 Nm.**

***Index Terms*—Disconnect unit, electromechanical actuator, electromagnetic actuator, magnetic coupling, permanent magnet generator, reliability, solenoid, more electric aircraft (MEA)**

I. Introduction

In recent years, interest has grown in converting existing non-propulsive systems on-board aircraft from mechanical, hydraulic, or pneumatic operation to fully electric operation [1]. Promoting such a trend, the overall mass of the aircraft is reduced and the power efficiency is increased, leading to lower fuel consumption, and reduced operating costs [2], [3]. As a result, aircraft power generation demands are exponentially increased [4], as well as the number of critical systems reliant on an uninterrupted electrical power supply. Therefore, the need to maximize the reliability of the electrical generation system becomes an important task.

A. Background

Permanent magnet (PM) generators represent a suitable solution for on-board aircraft electrical power generation due to their high power density [3], [5], [6]. As drawbacks, conventional PM machines feature a low fault tolerance [7], and lack the ability to

de-excite their field circuit unlike wound rotor synchronous machines. Thus, during an electrical failure on the PM generator side, the induced PM voltage will feed the fault (e.g., turn-to-turn short circuit) as long as the shaft is rotating. This uncontrolled condition can quickly escalate to a more severe fault (i.e., phase-to-ground and/or phase-to-phase short circuit) leading to generator downtime. Additionally, the ensuing current is a source of concern for PM demagnetization [8], [9], and winding insulation which may suffer undesired and premature thermal aging [10].

There is therefore a need to develop a protection system for newly implemented PM generators that is capable of disconnecting them from the aircraft turbines in the event of an electrical or mechanical fault. Generators are commonly connected to the gas turbine engine shaft via mechanical couplings [11]. This arrangement has the potential to cause damage to either the generator or the turbine if a severe fault occurs due to the transmission of speed/torque transients. Therefore, the fault escalation might be prevented by introducing a clutch. However mechanical clutches require frequent maintenance and are not efficient [12] and they also rely on hydraulic systems for control. These drawbacks make them unsuitable for more electric aircraft (MEA). Further, electromagnetic clutches need a continuous current supply to maintain the engaged position [13], which represents a power loss over time. Although hysteresis clutches operate without frictional contact interfaces, they are characterized by low torque to mass ratio, limited torque transmission (i.e., typically up to 12 Nm) and a lack of controllable disengagement.

B. Proposed EMA Concept

The standard mechanical coupling and/or the clutch can be replaced by the proposed electromechanical actuator (EMA) concept, which combines a coaxial magnetic coupling (CMC) and an electromagnetic actuator (EA) in one self-contained device. The CMC provides torque transmission, whereas the EA implements the disengagement function. The generation system architecture employing the proposed EMA is shown in Fig. 1, where one side of the EMA is coupled to the gas turbine shaft, while the other is connected to the PM generator shaft. The CMC allows for contactless torque transmission and provides passive protection against torque transients as its PMs are free to slip when the CMC's peak torque is exceeded [14], [15]. Additionally, the CMC reduces vibrations and is less sensitive to misalignment between coupled machines [16].

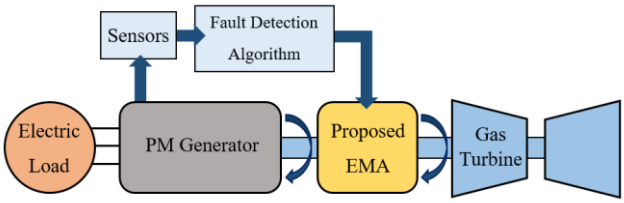

Fig. 1. System level architecture including the proposed EMA.

The fault detection algorithm monitors the status of the PM generator [17], [18]. If an electrical fault is detected, the EA is fed by DC voltage for a very short period, (i.e., disengagement time approximately 100 ms) and the magnetic field due to the resulting DC current creates an axial pull force. This pulling force is necessary to overcome the peak axial attraction force between the CMC

rings and it attracts the plunger towards the EA core causing the extraction of the inner PM ring from the outer one, disconnecting the PM generator from the turbine. The EMA side coupled to the turbine will keep rotating, while the generator side will gradually slow down due to the remaining PM field forces and frictional losses. Once the EMA shaft connected to the PM generator stops, no voltage is induced and the electrical fault is no longer sustained, preventing failure propagation. Both axial and rotational movement of the inner PM ring is enabled by mounting it to a ball spline assembly, which consists of a spline shaft and a spline nut. Additionally, the CMC is preferred to the axial magnetic coupling because it possesses a lower axial magnetic field strength and thus demands less pull force for disconnection.

In this paper, a novel EMA concept intended for a MEA application is discussed alongside its operating modes (i.e., engaged and disengaged modes). For each of the main EMA components, design considerations are given and their integration process is explained. Finally, the EMA prototype is manufactured and tested. The experimental results prove the effectiveness of the developed EMA in terms of both torque transmission capability and disengagement function.

II. EMA SPECIFICATIONS AND OPERATING MODES

The EMA prototype is designed to transmit torque in the engaged mode and allow disconnection from the turbine in case of a PM generator fault. Based on the specifications listed in Table I, two operating conditions, namely continuous duty (5,000 RPM and 32 Nm) and short-term (12,000 RPM and 9 Nm) duty are considered at the design stage.

TABLE I EMA DISCONNECT SYSTEM SPECIFICATIONS

Specification	Value
Continuous Mechanical Speed [RPM]	5,000
Continuous Torque [Nm]	32
Short-Term Mechanical Speed [RPM]	12,000
Short-Term Torque [Nm]	9

A. Operating Modes

The CMC consists of two coaxial rings (PM rings) equipped with a series of radially magnetized neodymium (N40) PMs mounted to the surface of stainless steel (grade 416) cores. In EMA engaged mode (i.e. in absence of electrical failure), the outer and inner PM rings of the CMC are axially aligned and rotate synchronously with a radial displacement angle depending on the transmitted torque. The EA consists of a ferromagnetic core hosting a DC excitation coil that surrounds the plunger. The ferromagnetic core and plunger are made of stainless-steel 416, while AWG 14 enameled round copper wire is used for the excitation coil. The plunger is mounted to the spline nut and is mechanically coupled to the inner PM ring. When the EMA operates in engaged mode, the EA's excitation coil is de-energized. When disengaged, the plunger ends its stroke by engaging with the mechanical latch. Once the EMA is disengaged, the EA's excitation coil is switched off and no torque is transferred from the turbine to the PM generator. The exploded view of the proposed EMA is reported in Fig. 2 where its sub-components are shown.

This article has been accepted for publication in IEEE Transactions on Transportation Electrification. This is the author's version which has not been fully edited and content may change prior to final publication. Citation information: DOI 10.1109/TTE.2022.3233538

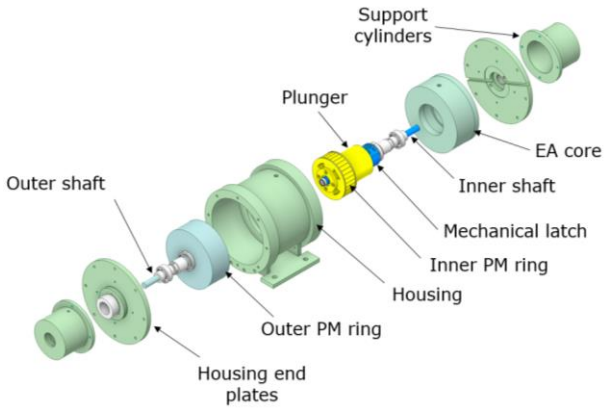

Fig. 2. EMA prototype exploded view.

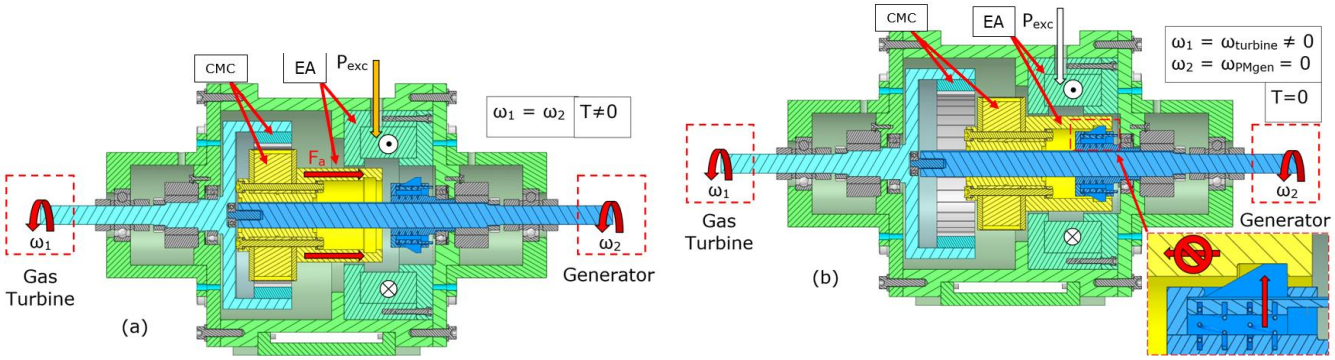

Fig. 3. Cross sectional view through EMA (set for 100 Nm peak torque): (a) engaged operating mode, (b) disengaged operating mode.

The EMA housing is made of aluminium alloy to reduce the total mass and isolate the rest of the EMA from potential interferences caused by the EA magnetic field. Fig. 3 shows the cross-sectional view of the EMA in both its operating modes, namely engaged and disengaged modes. In particular, Fig. 3a considers the engaged operating mode where the inner and outer PM rings of the CMC are aligned, and contactless torque transmission takes place, while the speed of the outer shaft (ω1) is equal to the speed of the inner shaft (ω2). In EMA engaged mode, the EA's excitation coil is not energized, and the EA joule losses are null.

The EMA disengaged operating mode is illustrated in Fig. 3b, where the inner PM ring is located outside the outer PM ring, whereas the EA's plunger is completely retracted and locked in position by the mechanical latch. In EMA disengaged mode, the inner shaft speed (ω2) decreases due to the absence of torque transfer, whilst the outer shaft speed (ω1) remains the same as it was prior to disconnection. It is worth noting that the outer shaft speed (ω1) will be subject to a transient just after disconnection due to the sudden change in load. In particular, ω1 increases for a short period although the speed perturbation is contained due to the relatively large inertia of the turbine rotor. The main components of both the inner and outer shafts are reported in Fig. 4.

This article has been accepted for publication in IEEE Transactions on Transportation Electrification. This is the author's version which has not been fully edited and content may change prior to final publication. Citation information: DOI 10.1109/TTE.2022.3233538

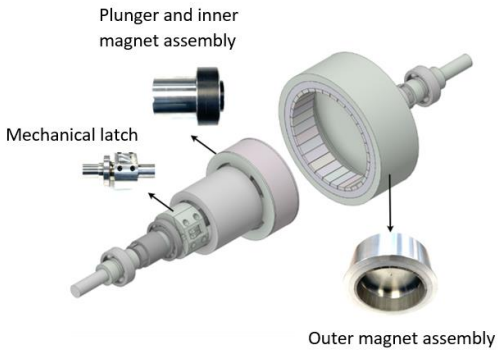

Fig. 4. Inner and outer shaft assemblies.

The EMA can be coupled either way around, although it is preferable to connect the outer PM ring to the gas turbine engine. This choice would prevent undesirable voltage being induced in the ferromagnetic parts after EMA disengagement, avoiding additional hysteresis and eddy current losses, as the inner PM ring will stop rotating. Therefore, the outer PM ring and its shaft are coupled to the gas turbine engine and stay in the same axial position in both operating modes. Conversely, the inner assembly (i.e., inner PM ring and plunger), whose shaft is coupled to the PM generator, is free to axially move towards the mechanical latch.

B. Re-engagement Operation

The EMA is designed to inhibit re-engagement while the aircraft is still flying because the electric failure on the PM generator might persist and priority to the safety of the overall electrical system must be given. Thus, once the EMA disengagement is triggered and completed, the spring-loaded latch tongues return to their original position and the plunger is locked in place. Since the PM generator will no longer produce any electrical power over the remaining flight time, electrical load reconfiguration is required according to a predetermined priority order [19], [20].

After aircraft landing, a full diagnostic check of the PM generator is performed to detect and remove the fault. Only at this stage, the EMA re-engagement is manually carried out by depressing the extensions on the ends of the latch tongues and releasing the plunger from the latch. The EMA re-engagement takes place under the action of the residual attraction force between the PM rings. For reducing the downtime, a remote release system can be implemented on a future version of the EMA.

C. Peak Torque Adjustment Feature

As shown in Fig. 3a, the inner PM ring self-locates within the outer PM ring due to PM attraction and no extra mechanism is required to hold the inner PM ring in position. When the PM rings are axially aligned (i.e., zero offset), the CMC is designed to develop a peak torque of 100 Nm, but this value can be reduced by increasing the axial displacement between the PM rings for the engaged mode. The peak torque adjustment feature is controlled by rotating the locknut at the end of the spline shaft, as shown in Fig. 5a. The peak torque as function of the axial offset is illustrated in Fig. 5b and its value can be set in the range 0-100 Nm,

allowing the fine-tuning of the CMC peak/slip torque. Such a feature enhances the functional flexibility of the EMA without significantly increasing its overall mass.

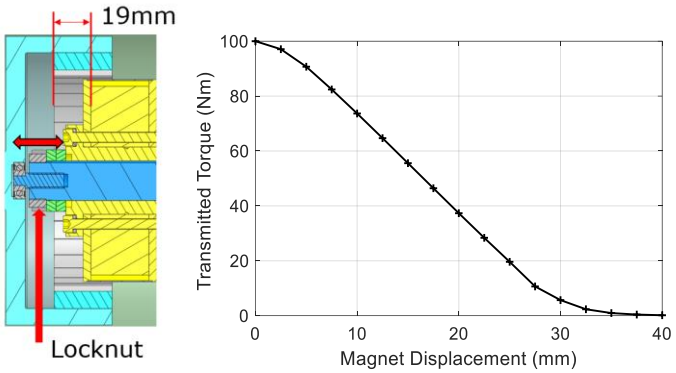

(a) (b)

Fig. 5. Peak torque adjustment feature: (a) Inner PM ring with 19 mm axial, (b) Peak torque (Nm) vs. PM ring offset (mm).

The peak torque can be adjusted to avoid nuisance slip events that could be triggered by infrequent rogue transient events which would ordinarily not pose a risk to the integrity of the generation system (i.e. set to a few Nm above the peak torque). The peak torque adjustment feature is included primarily to validate the magneto static analysis results for different values of peak static torque that are reported in section III B. Based on the specifications given in Table I, a 40 Nm peak torque is set by adjusting the axial offset to 19 mm to ensure the safe transmission of 32 Nm at 12,000 RPM.

III. EMA Components Design, Manufacture, and Assembly

A. Housing

The CMC and EA must be combined in a practical and functional assembly, which can support the applied loads and maintain alignment between the shafts. To this end, the shafts are housed within an aluminium structure, which provides bearing support to the inner and outer shafts and isolates the rotating assembly from the surrounding environment. The housing is composed of three parts: the main body, the end plates and the support cylinders. The inner and outer shafts' bearings are supported on the housing end plates and support cylinders, which in turn are fastened to the main housing body. Two resolvers are installed for measuring the rotational speed and angular displacement between inner and outer PM rings.

B. Coaxial Magnetic Coupling

The CMC is designed for developing a maximum peak torque of 100 Nm (zero axial offset) although its operating value can be adjusted as discussed in Section II C. The CMC optimum geometry is determined with the purpose of maximizing the torque to mass ratio through the methodology used in [21]. The main geometric and performance parameters of the CMC are listed in Table II.

This article has been accepted for publication in IEEE Transactions on Transportation Electrification. This is the author's version which has not been fully edited and content may change prior to final publication. Citation information: DOI 10.1109/TTE.2022.3233538

TABLE II CMC PARAMETERS

Parameter	Value
Pole-Pair Number	32
Permanent Magnet Thickness [mm]	4
Airgap Thickness [mm]	2.5
Axial Length [mm]	30
Outer Diameter [mm]	133
Total Mass [kg]	2.63
Rated Peak Torque [Nm]	100
Chosen Offset Peak Torque [Nm]	40
PM Ring Offset Distance [mm]	19

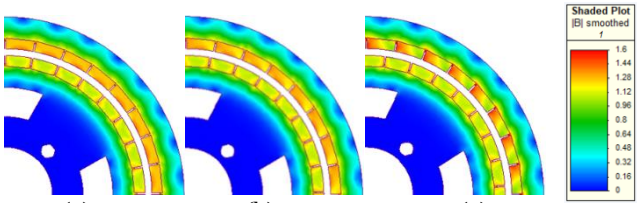

Fig. 6. CMC flux density plots (axial offset 19 mm): (a) no-load, (b) 9 Nm at 12,000 RPM, and (c) 32 Nm at 5,000 RPM.

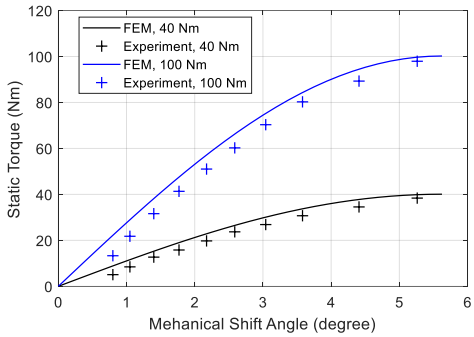

Fig. 7. CMC static torque versus angular displacement.

The initial geometry of the 2D CMC was obtained using an analytical tool [22], [23] based on Maxwell's and Poisson's equations to define the optimum dimensions of the magnets for a peak torque transmission capacity of 100 Nm. 2D finite element (FE) simulations were then performed to verify the CMC performance at the main operating points (see Table I). The PM geometries on the inner and outer magnets are set to neodymium N40 and the inner magnet is rotated until the peak torque value is obtained. Considering an axial offset such as to produce a static peak torque of 40 Nm, the flux density plot corresponding to the following operating conditions: a) no-load, b) 9 Nm at 12,000 RPM, and c) 32 Nm at 5,000 RPM are given in Fig. 6. The FE results conclude that the CMC does not experience heavy magnetic saturation under the most challenging operating condition.

The peak torque of the CMC design is experimentally validated by applying a measured torque to one of the EMA shafts and fixing the other shaft in place on a static test rig. The FE simulation results regarding the peak static torque as a function of the shift angle are compared with those experimentally collected on the EMA prototype. The outcome of such a comparative exercise is reported in Fig. 7, where two different axial offsets (i.e., 100 Nm and 40 Nm peak torque) are evaluated. The mechanical shift

angle associated with the peak static torque is equal to 5.625° and does not change with the axial offset, since its value depends on the pole pair number. The results in Fig. 7 confirm that the CMC prototype can transfer the desired target torque regardless of the axial offset selected. The mismatch between simulation and experimental findings can be ascribed to the 2D nature of the FE model. The error between the analytical and experimental value of peak static torque is 2.5% in both the 100 Nm and 40 Nm cases.

C. Inner and Outer Magnet Assembly

In Fig. 8, the inner magnet assembly is shown and its main subcomponents are: the inner PM ring, the inner magnet core, shaft collars, spline nut, and the plunger. The entire inner magnet assembly is fastened together with bolts through the flange on the spline nut. The radially magnetized PMs are glued on the surface of the inner CMC core, while a carbon fiber sleeve tightly wraps the inner PM ring providing pre-load to the PMs against the inertial radial forces.

The outer magnet assembly contains the outer PM ring and outer PM core, its exploded view is depicted in Fig 9. The PMs are bonded to the ferromagnetic core, which is pressed into the outer shaft to prevent its separation from the rotor assembly when the inner magnet assembly is retracted (i.e., during EMA disconnection).

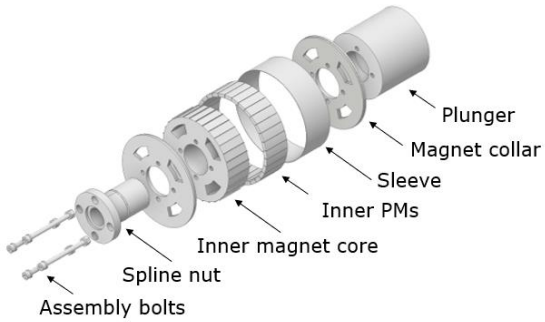

Fig. 8. Exploded view of the inner magnet assembly.

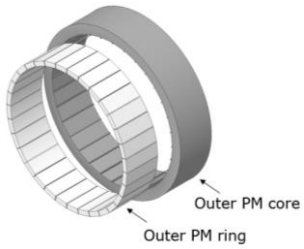

Fig. 9. Exploded view of the outer magnet assembly.

D. Electromagnetic Actuator

The EA consists of a movable plunger coupled to the inner PM ring and a ferromagnetic core pressed into the housing's main body. An air gap of 2 mm thickness allows the plunger to travel through the EA core when a DC current flows through the excitation coil. The EA core mounts a removable cover that enables easy assembly and holds in place the excitation coil. The latter is obtained

using a grade 2, AWG 14, round copper enameled wire with 200°C thermal class. Due to the short operational time (i.e. about 100 ms), the excitation coil is characterized by low energy consumption and high overload capability. The fully assembled EA is shown in Fig. 10 together with an exploded view.

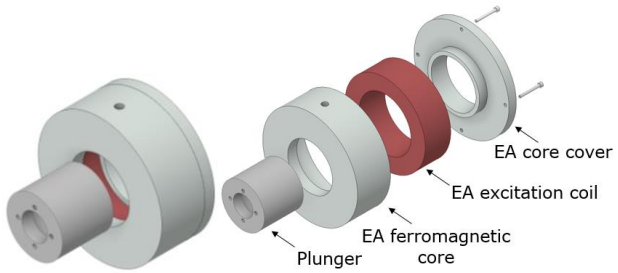

Fig. 10. EA geometry: (a) assembled view, (b) exploded view.

The EA design was created by using a 2D FE transient magnetic model developed with Simcenter MAGNET to adjust the dimensions of the EA core and coil. The geometry that produced an axial pull force across the full stroke distance that exceeded the equivalent CMC axial attraction force for a maximum input current of 15 A was selected as shown in Fig. 6. The main EA parameters are summarized in Table III. Considering the peak torque adjustment feature, the total stroke length (axial distance from engage to disengage EMA mode) is equal to 36 mm when the PM ring offset is null (i.e., 100 Nm peak torque). On the other hand, 17 mm of stroke length is necessary for EMA disengagement when the PM ring offset is set to 19 mm (i.e. 40 Nm peak torque). Flux density plots and the flux lines resulting from a 15 A DC current are shown in Fig 11(a) for two core-plunger axial displacements (i.e., 0 and 36 mm).

Table III EA PARAMETERS

Parameter	Value
Actuator Core Axial Length [mm]	71
Actuator Core Outer Dimeter [mm]	167
Starting Force [N]	225
Peak Force [N]	532
Current Density [A/mm^2]	8
Rated Current [A]	15
Rated Voltage [V]	24
Slot Copper Fill Factor	0.5
Number of Turns	300
Wire Size	AWG 14
Joule Losses [W]	414

The axial force produced by the EA (EA force) is compared to the force needed to extract the inner PM ring (CMC force) in order to verify that the EA force is greater than the CMC force across the full stroke distance. The fulfillment of the condition EA force > CMC force ensures the successful EMA disengagement. The CMC force depends on 1) the axial displacement between PM rings and 2) the torque transferred by the CMC. As the transmitted torque decreases, the axial force required to pull the inner PM ring increases. Thus, the most challenging EMA disconnection condition occurs when the CMC operates with a low transmitted torque (i.e. 0 Nm). In Fig 11(b), the trends of both EA force and CMC force as a function of the core-plunger axial displacement are illustrated.

This article has been accepted for publication in IEEE Transactions on Transportation Electrification. This is the author's version which has not been fully edited and content may change prior to final publication. Citation information: DOI 10.1109/TTE.2022.3233538

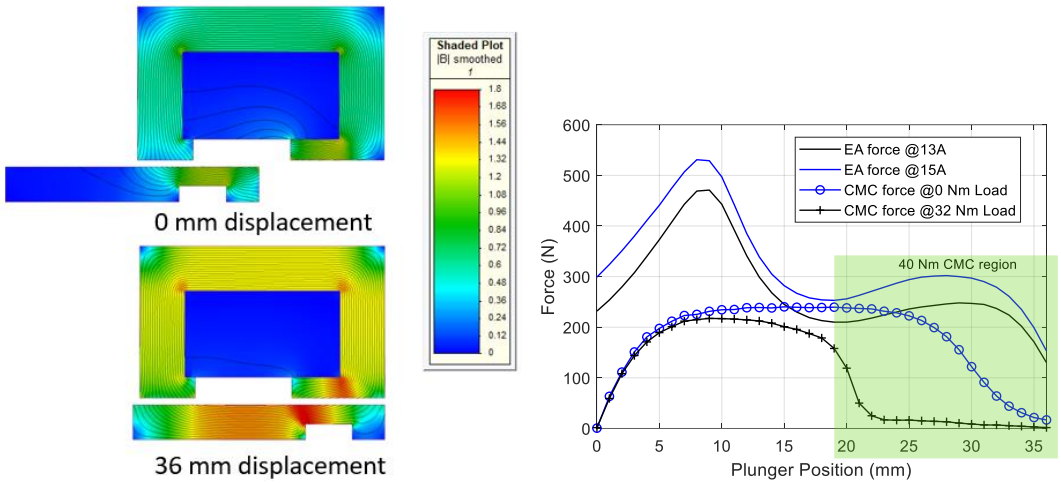

(a) (b)

Fig. 11. EA FE results: (a) flux density plots of the EA at 0 mm and 36 mm displacements when a 15 A current is applied, and (b) EA axial force and CMC axial force as a function of the plunger position.

Two values of CMC force (i.e. at 0 and 32 Nm loads) are investigated, and the EA force is determined throughout the full stroke of 36 mm by considering two DC current values (i.e. 13 A and 15 A). The FE results in Fig 11(b) show that disconnection is achieved when a current of 15 A is supplied when the load is 32 Nm for both 0 and 19 mm offset positions. Disconnection is also achieved for both positions when the load is 0 Nm for a lower current of 13 A. The green shaded region represents the EA operating region when the PM ring offset is set to 19 mm.

E. Mechanical Latch

The mechanical latch consists of a main body pressed on the inner shaft and two spring-loaded latch tongues, as depicted in Fig. 12. A shaft mounted latch configuration is preferred to a housing mounted latch to avoid frictional wear and extra design complexity. The latch design also provides a seating position for the inner shaft to housing bearing and an abutment for the resolver. When the plunger is locked (i.e., EMA disengaged mode), a residual attraction force of 16 N exists between the PM rings. This force is enough to allow EMA re-engagement once the latch is released. The latch is mounted directly to the inner shaft, as a result, the plunger and latch do not rotate relative to one another. Therefore, once the system is disconnected and the plunger is pulled back to connect with the latch, no frictional wearing occurs due to rotation. The latch is only released and the EMA reengaged once the aircraft is on the ground, the generator has been checked and the electrical fault has been resolved.

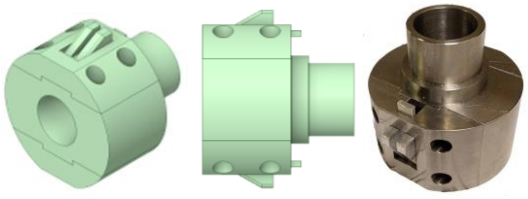

(a) (b) (c)

Fig. 12. Latch geometry: (a) isometric view, (b) right side view, (c) manufactured latch.

F. Inner and outer shaft assemblies

The inner shaft assembly supports the inner PM ring and is formed from a 20 mm ball spline shaft, which retains the flanged spline nut as shown in Fig. 13(a). The spline nut supports the inner PM ring and the plunger, while the shaft is machined to accommodate the mechanical latch, the bearings and the resolver rotor. The inner shaft assembly in the engaged position is illustrated in Fig. 13(b). The primary function of the outer shaft assembly is to support the outer PM ring, as shown in Fig. 14. The outer shaft contains a recess in which the inner to outer rotor bearing is pressed, providing support to the free end of the inner PM ring. Both inner and outer shafts have a minimum diameter of 15 mm, which is compatible with the maximum peak static torque of 100 Nm.

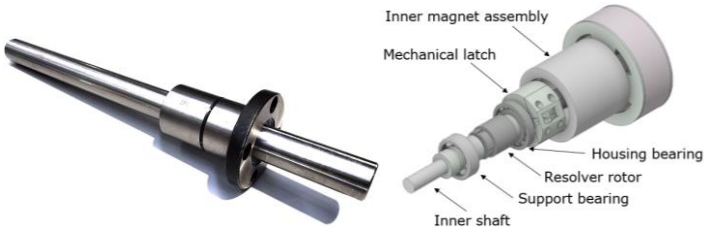

Fig. 13. Inner shaft assembly: (a) ball spine shaft (pre-machined), and (b) complete assembly.

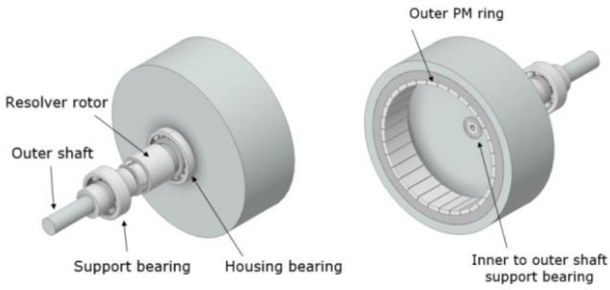

Fig. 14. Outer shaft assembly: (a) rear view, (b) front view.

G. Bearing arrangement

Angular bearing misalignment between the rotors and the housing presents a source of concern, since it exposes the bearings to high axial and radial cyclical stresses that could lead to mechanical failures. In the designed EMA, both the inner and outer shafts are supported by a pair of deep groove ball bearings, which guarantee two points of contact that help to maintain coaxial alignment. The main bearings (type 16005) are located inside the housing end plates (number 2 in Fig. 15), while the support bearings (type 6302) are situated within support cylinders attached to the housing (number 1 in Fig. 15). An additional bearing (type 635-2Z) is placed between the shafts' ends (number 3 in Fig. 15) to keep a constant CMC air gap and prevent rotor misalignment due to the radial attraction force of the PMs. All bearings are rated at 20,000 RPM and they are arranged to allow independent shaft rotation when EMA disengagement takes place.

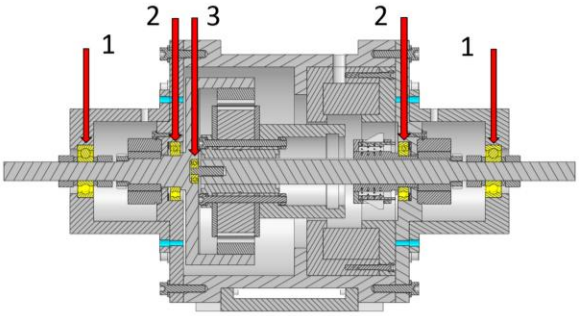

Fig. 15. Bearing locations: support bearings (1), housing bearings (2), inner to outer shaft support bearing (3).

H. Torque to mass ratio comparison

Magnetic couplings cannot transfer as much torque as comparably sized physical couplings/clutches due to the contactless nature of their operation. However, once the mass of the rotors, housing and disconnection systems are taken into account, the EMA becomes more competitive in terms of torque to mass ratio. The assembled prototype of the EMA has a torque to mass ratio of 3.86 Nm/kg, which is similar to existing examples of commercially available, independent mechanical and electromagnetic clutch units. The torque to mass ratio of the EMA and existing clutch/brake units is given in Table IV for comparison purposes.

Table IV COMPARISON OF TORQUE TO MASS RATIO

Model	Torque (Nm)	Torque to Mass Ratio (Nm/kg)
EMA	100	3.86
JBJ – MSU single disk [24]	100	3.92
ABSSAC – 125-16-12G [25]	80	3.64
Mayr – ROBA takt [26]	80	5.23

IV. EMA PROTOTYPE EXPERIMENTAL TESTING

Following the design stage, the EMA prototype is manufactured and its key mass and geometric properties are given in Table V. Experimental tests are performed on the EMA prototype to evaluate the magnetic and mechanical performance. The first aim on the test campaign is to prove the concept by verifying the torque transmission capability at both operating points (32 Nm at 5,000 RPM and 9 Nm at 12,000 RPM). The second aim is to assess the disconnection function at 12,000 RPM and zero transmitted torque (i.e., worst operating condition). As described in Section III D, the most challenging operating condition for EMA disengagement occurs at zero transfer torque, when the CMC angle shift is 0^o and the maximum axial coupling force is established. Testing the EMA disengagement at zero transmitted torque ensures that the disconnection function works properly under all other transfer torque values.

Table V EMA PROTOTYPE PARAMETERS

Parameter	Value
Housing Length [mm]	212.55
Housing Width [mm]	210
Housing Height [mm]	210
EMA Total Mass [kg]	25.93
EMA Housing Mass [kg]	7.2
Outer Shaft Assembly Mass [kg]	4.36
Outer Magnet Ring Mass [kg]	1.13
Inner Shaft Assembly Mass [kg]	4.63
Inner Magnet Assembly Mass [kg]	2.8
EA Core + Coil Mass [kg]	8.43

A. Validation of Torque Transmission Capability

For testing purposes, the EMA prototype is placed between two twin 49 kW electric drives, as illustrated in Fig. 16, where the first electric drive is speed controlled (i.e. drive motor), while the other is torque controlled (i.e. load motor). Each electric drive consists of an asynchronous motor fed by a commercial power converter and a graphical user interface is used for inputting the set point values. A torque transducer mechanically joins the EMA's outer shaft to the drive motor and measures the transferred torque. The test campaign is carried out considering an axial offset of 19 mm for the CMC's PM rings, which corresponds to 40 Nm of transmitted peak torque.

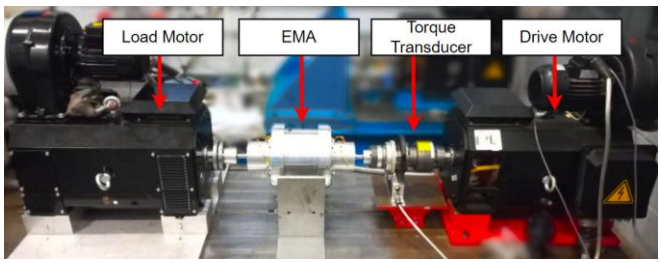

Fig. 16. Experimental setup for testing the EMA prototype.

In Fig. 17, the measured speed and torque profiles relative to the highest torque operating point (32 Nm at 5,000 RPM) are reported. During the test, the system speed is first increased up to 5,000 RPM and then the target torque of 32 Nm is applied. Under this condition, the EMA prototype confirms its capability of transferring the highest torque value as specified in Table I. The highest speed operating point is also tested and the collected results are provided in Fig. 18. The system speed is ramped up to 12,000 RPM under the no-load condition and once the reference speed is reached, a 9 Nm load torque is applied. The collected results prove that the EMA prototype is able to operate at the demanded maximum speed and torque conditions with no loss of CMC's synchronicity. In both operating points, the mechanical CMC angle shift is measured and compared to the corresponding simulated value for design validation purpose. The recorded results are listed in Table VI and apart from a slightly mismatch, they are in line with the design expectations.

This article has been accepted for publication in IEEE Transactions on Transportation Electrification. This is the author's version which has not been fully edited and content may change prior to final publication. Citation information: DOI 10.1109/TTE.2022.3233538

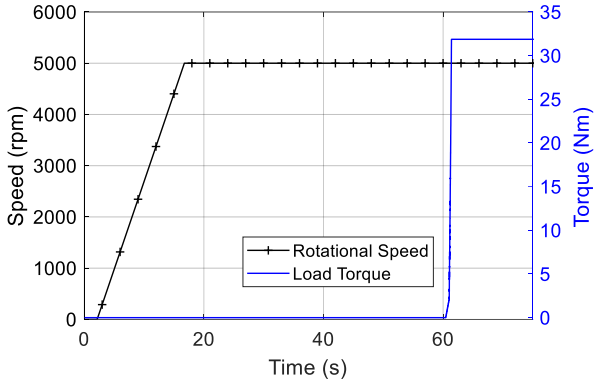

Fig. 17. Measured speed and torque profiles for validating the first operating point (i.e., 32 Nm at 5,000 RPM).

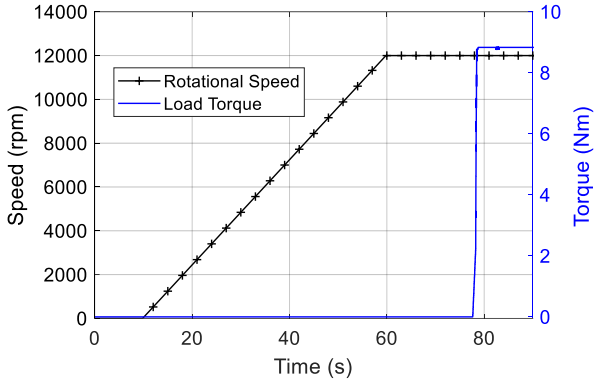

Fig. 18. Measured speed and torque profiles for validating the second operating point (i.e., 9 Nm at 12,000 RPM).

TABLE VI EXPERIMENTAL AND ANALYTICAL DISPLACEMENT ANGLE VALIDATION

Operating point	Torque (Nm)	Simulation result (Mech. degrees °)	Experimental result (Mech. degrees °)
1	32	3.23	3.3
2	9	0.75	0.9

At 12,000 RPM, the support bearing temperature is monitored using a thermal camera and an average maximum steady-state temperature of 57.8 ºC is reached at both ends of the EMA. The thermal images of the support cylinder bearings at 12,000 RPM are depicted in Fig 19.

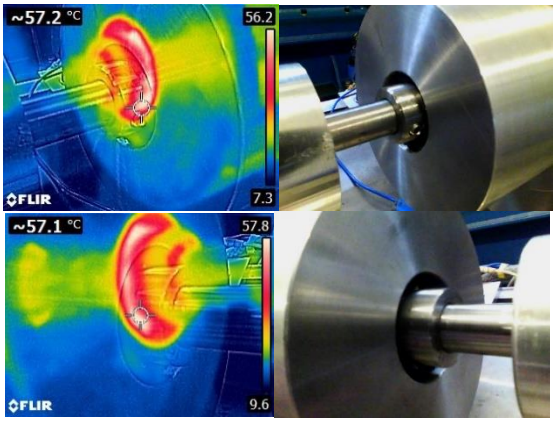

Fig. 19. Steady-state bearing temperatures at 12,000 RPM.

B. Disconnection Function Validation

With EMA performance verified in the engaged mode, the disengagement function is then tested, employing same test setup as in Fig. 16. In the laboratory environment, the AE's excitation coil is supplied through an 80 V, 120 A DC power supply controlled via a manual switch, which replaces the automatic switch driven by the fault diagnostic algorithm of the actual application. Preliminary disconnection tests carried out at speed values lower than 12,000 RPM reveal that (as expected) the rotational speed does not affect the EMA disengagement performance. Instead, the transmitted torque has the most influence on the axial force required to accomplish the EMA disengagement, as previously discussed.

The first disconnection test is performed at 12,000 RPM with no-load applied. The system is accelerated to the target speed of 12,000 RPM and the EA's excitation coil is then energized. The corresponding results are given in Fig. 20, where the speed plots of both drive and load machines are shown. The EMA disengagement occurs at 48.7 s, causing the load motor slow-down due to bearing friction and air resistance, while the drive motor set point is reduced to 0 RPM just 10 s after the latch is engaged. If the load side of the EMA was connected to a PM generator that experienced a short-circuit fault, it would slow down at a much faster rate than in this experiment as the PM generator rotor would be physically disconnected from the drive side the moment that the EMA is disengaged. The input mechanical power to the PM generator would be immediately reduced to nothing and the residual stator currents in the PM would act to brake the PM rotor.

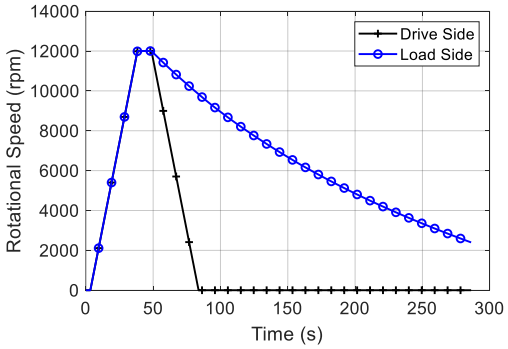

Fig. 20. Measured speed profiles during disconnection test at 12,000 RPM and no-load.

The experimental voltage and current waveforms of EA's excitation coil during the EMA disengagement event are shown in Fig. 21a. The DC current flowing through the excitation coil reaches a peak of 25 A before its value stabilizes at 13 A. In Fig. 21a, the measured DC current trend is also compared against that obtained through FE simulation. The disengagement transient in terms of EA and CMC forces is reported in Fig. 21b along with the plunger position. The EA's excitation coil is supplied over a period of 100 ms, although the plunger travel time is only 28.5 ms (green shaded area in Fig. 21b). Indeed, the plunger starts moving as soon as the EA force exceeds the resisting CMC force (91.5 ms in Fig. 21b).

This article has been accepted for publication in IEEE Transactions on Transportation Electrification. This is the author's version which has not been fully edited and content may change prior to final publication. Citation information: DOI 10.1109/TTE.2022.3233538

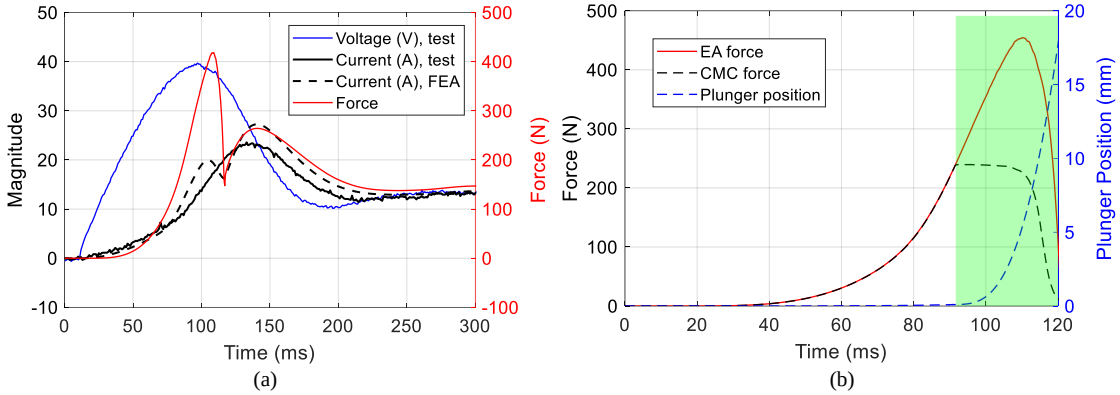

Fig. 21. EMA disengagement at 12,000 RPM and no load: (a) voltage and current of the EA's excitation coil (b) force and plunger position (19 mm offset).

The disconnection test at no-load revealed that an electrical power higher than 195 W (FE simulation result) is required during the transient to achieve successful disconnection. This required power can be reduced by slightly increasing the transmitted torque just prior the EMA disengagement is triggered, which may occur regardless in the event of a severe electrical fault. Indeed, higher values of transmitted torque leads to lower CMC axial resistant force, as illustrated in Fig. 11a.

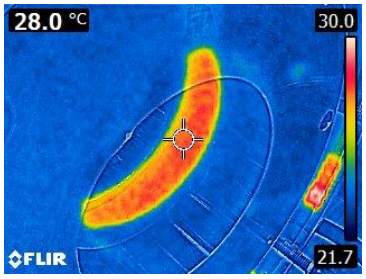

Fig. 22. EA excitation coil temperature with 13 A for 30 s.

Although the short operating time of the EA excitation coil makes both heating effects and power consumption negligible, a thermal test is performed since the transient electric power is higher than expected. During the thermal test, the EA excitation coil, which features a 1 Ω resistance, is fed by 13 A DC current over a 30 s timespan. The thermal test results are shown in Fig. 22, where a peak temperature of 28°C is reached, which is well below the maximum value for wire's thermal class.

V. Conclusions And Further Work

In this work, a novel EMA concept is designed, analysed and tested. The proposed EMA is intended for use in an MEA application to decouple the aircraft power generation system on command in response to the detection of electrical faults. The EMA offers some key advantages over existing mechanical and electromagnetic clutch and coupling alternatives for coupling the PM generator to the turbine engine that are summarized as follows. The EMA concept is simple and compact due to the integration of the CMC and EA in one device, i.e. no hydraulic systems are required to operate the EMA. There is no frictional wear between the rotating components of the EMA due to contactless torque transfer through the CMC, thus inspection and maintenance time

and cost is reduced. The EMA provides improved electrical efficiency over electromagnetic clutches due to the short operating time of the EA excitation coil and the peak torque adjustment feature enables the selection of the slip torque protection level.

The CMC and EA components were designed and analysed using 2DFE magnetic models to develop a system capable of transferring a peak torque of 100 Nm through the CMC and capable of producing enough axial pull force in the EA to decouple the CMC. A prototype of the EMA was built and static tests were performed to analyze the accuracy of the 2DFE model when the peak torque was set to 100 Nm and 40 Nm. The analytical peak torque results were accurate to within 2.5%. The 2DFE models also accurately predicted that the CMC (when set to 40 Nm) would be decoupled when the EA force exceeded 250 N, as validated by a disconnection test performed on the EMA prototype.

The EMA prototype was tested and the experimental results confirmed EMA's ability to transfer torque at two distinct operating points, namely 32 Nm at 5,000 RPM and 9 Nm at 12,000 RPM. The disconnection capability was verified in the most challenging operating condition, i.e., 12,000 RPM at no-load, confirming fast response and complete disconnection capability during zero-torque transmission.

The EA and housing make up a significant proportion of the EMA total mass (60.3%). Therefore, future efforts are to be focused on optimizing the mass of these components with the purpose of further improving the torque to mass ratio. The effects of increased axial force between the inner and outer magnet assemblies in the PM due to the peak torque adjustment feature should also be explored in further detail should this feature be incorporated beyond experimental prototypes.

ACKNOWLEDGEMENT

This work was supported by the Clean Sky 2 Joint Undertaking through the European Union's Horizon 2020 Research and Innovation Programme under Grant 807081 and Grant 821023.

REFERENCES

[1] J. A. Rosero, J. A. Ortega, E. Aldabas, and L. Romeral, 'Moving towards a more electric aircraft', *IEEE Aerosp. Electron. Syst. Mag.*, vol. 22, no. 3, pp. 3–9, Mar. 2007, doi: 10.1109/MAES.2007.340500.

[2] B. Sarlioglu and C. T. Morris, 'More Electric Aircraft: Review, Challenges, and Opportunities for Commercial Transport Aircraft', *IEEE Trans. Transp. Electrification*, vol. 1, no. 1, pp. 54–64, Jun. 2015, doi: 10.1109/TTE.2015.2426499.

[3] S. Bozhko *et al.*, 'Development of Aircraft Electric Starter–Generator System Based on Active Rectification Technology', *IEEE Trans. Transp. Electrification*, vol. 4, no. 4, pp. 985–996, Dec. 2018, doi: 10.1109/TTE.2018.2863031.

[4] V. Madonna, P. Giangrande, and M. Galea, 'Electrical Power Generation in Aircraft: Review, Challenges, and Opportunities', *IEEE Trans. Transp. Electrification*, vol. 4, no. 3, pp. 646–659, Sep. 2018, doi: 10.1109/TTE.2018.2834142.

[5] Z. Xu, A. L. Rocca, S. J. Pickering, C. Eastwick, C. Gerada, and S. Bozhko, 'Mechanical and thermal design of an aeroengine starter/generator', in *2015 IEEE International Electric Machines & Drives Conference (IEMDC)*, Coeur d'Alene, ID, May 2015, pp. 1607–1613. doi: 10.1109/IEMDC.2015.7409278.

[6] A. M. EL-Refaie, M. R. Shah, and K.-K. Huh, 'High-Power-Density Fault-Tolerant PM Generator for Safety-Critical Applications', *IEEE Trans. Ind. Appl.*, vol. 50, no. 3, pp. 1717–1728, May 2014, doi: 10.1109/TIA.2013.2282852.

[7] W. Zhao, L. Xu, and G. Liu, 'Overview of permanent-magnet fault-tolerant machines: Topology and design', *CES Trans. Electr. Mach. Syst.*, vol. 2, no. 1, pp. 51–64, Mar. 2018, doi: 10.23919/TEMS.2018.8326451.

[8] B. Wang, G. Vakil, Y. Liu, T. Yang, Z. Zhang, and C. Gerada, 'Optimization and Analysis of a High Power Density and Fault Tolerant Starter–Generator for Aircraft Application', *Energies*, vol. 14, no. 1, p. 113, Dec. 2020, doi: 10.3390/en14010113.

[9] B. Wang, Y. Liu, G. Vakil, T. Yang, and Z. Zhang, 'Feasibility of Permanent Magnet Fault Tolerant Machines for Aircraft Starter/Generator Systems', in *2020 International Conference on Electrical Machines (ICEM)*, Gothenburg, Sweden, Aug. 2020, pp. 2104–2110. doi: 10.1109/ICEM49940.2020.9270965.

[10] P. Giangrande, V. Madonna, S. Nuzzo, and M. Galea, 'Moving Toward a Reliability-Oriented Design Approach of Low-Voltage Electrical Machines by Including Insulation Thermal Aging Considerations', *IEEE Trans. Transp. Electrification*, vol. 6, no. 1, pp. 16–27, Mar. 2020, doi: 10.1109/TTE.2020.2971191.

[11] P. Wheeler and S. Bozhko, 'The More Electric Aircraft: Technology and challenges.', *IEEE Electrification Mag.*, vol. 2, no. 4, pp. 6–12, Dec. 2014, doi: 10.1109/MELE.2014.2360720.

[12] G. Gallicchio, M. D. Nardo, M. Palmieri, and F. Cupertino, 'Analysis, Design and Optimization of Hysteresis Clutches', *IEEE Open J. Ind. Appl.*, vol. 1, pp. 258–269, 2020, doi: 10.1109/OJIA.2020.3042884.

[13] J. Wu, Q. Li, D. Song, L. Yang, F. Cheng, and X. Liang, 'Energy Saving Analysis Using Pulse Width Modulation Techniques Controlling Electromagnetic Clutch in EPS System', in *2009 Asia-Pacific Conference on Information Processing*, Shenzhen, China, Jul. 2009, pp. 394–397. doi: 10.1109/APCIP.2009.106.

[14] O. Tweedy, Y. Akcay, P. Giangrande, and M. Galea, 'Magneto-mechanical Design and Development of a Coaxial Magnetic Coupling with Optimization of Torque to Mass Ratio', in *2021 IEEE International Electric Machines & Drives Conference (IEMDC)*, Hartford, CT, USA, May 2021, pp. 1–8. doi: 10.1109/IEMDC47953.2021.9449544.

[15] T. Lubin, S. Mezani, and A. Rezzoug, 'Simple Analytical Expressions for the Force and Torque of Axial Magnetic Couplings', *IEEE Trans. Energy Convers.*, vol. 27, no. 2, pp. 536–546, Jun. 2012, doi: 10.1109/TEC.2012.2183372.

[16] L. Belguerras, S. Mezani, and T. Lubin, 'Analytical Modeling of an Axial Field Magnetic Coupler With Cylindrical Magnets', *IEEE Trans. Magn.*, vol. 57, no. 2, pp. 1–5, Feb. 2021, doi: 10.1109/TMAG.2020.3005949.

[17] C.-C. Hsu and S.-C. Yang, 'Permanent-Magnet Machine Flux and Torque Response Under the Influence of Turn Fault', *IEEE Trans. Ind. Electron.*, vol. 67, no. 1, pp. 169–179, Jan. 2020, doi: 10.1109/TIE.2019.2891398.

[18] S. Choi *et al.*, 'Fault Diagnosis Techniques for Permanent Magnet AC Machine and Drives—A Review of Current State of the Art', *IEEE Trans. Transp. Electrification*, vol. 4, no. 2, pp. 444–463, Jun. 2018, doi: 10.1109/TTE.2018.2819627.

[19] C. Spagnolo, S. Sumsurooah, C. I. Hill, and S. Bozhko, 'Smart Controller Design for Safety Operation of the MEA Electrical Distribution System', in *IECON 2018 - 44th Annual Conference of the IEEE Industrial Electronics Society*, D.C., DC, USA, Oct. 2018, pp. 5778–5785. doi: 10.1109/IECON.2018.8591132.

[20] C. Spagnolo, S. Sumsurooah, C. I. Hill, and S. Bozhko, 'Finite state machine control for aircraft electrical distribution system', *J. Eng.*, vol. 2018, no. 13, pp. 506–511, Jan. 2018, doi: 10.1049/joe.2018.0039.

[21] Y. Akcay, P. Giangrande, C. Gerada, and M. Galea, 'Comparative Analysis Between Axial and Coaxial Magnetic Couplings', in *The 10th International Conference on Power Electronics, Machines and Drives (PEMD 2020)*, Online Conference, 2021, pp. 385–390. doi: 10.1049/icp.2021.1147.

[22] Y. Akcay, P. Giangrande, O. Tweedy, and M. Galea, 'Fast and Accurate 2D Analytical Subdomain Method for Coaxial Magnetic Coupling Analysis', *Energies*, vol. 14, no. 15, p. 4656, Jul. 2021, doi: 10.3390/en14154656.

[23] T. Lubin, S. Mezani, and A. Rezzoug, 'Analytical Computation of the Magnetic Field Distribution in a Magnetic Gear', *IEEE Trans. Magn.*, vol. 46, no. 7, pp. 2611–2621, Jul. 2010, doi: 10.1109/TMAG.2010.2044187.

[24] 'Electromagnetic Clutches and Brakes from JBJ Tecniques Limited'. https://www.jbj.co.uk/e-publications/Electromagnetic_clutches-from-jbj-Techniques-Limited/28/ (accessed Mar. 31, 2022).

[25] 'Abssac Electromagnetic Clutch and Brake Units'. https://www.abssac.co.uk/uploads/docs/8yulrpls_Clutch_and_Brake_Units.pdf (accessed Mar. 31, 2022).

[26] 'Mayr Electromagnetic Clutches and Brakes, Clutch Brake Units'. https://www.mayr.com/produkte/dokumentationen/k_500_v10_en_09_11_2016.pdf (accessed Mar. 31, 2022).